

# Geophysical Research Letters



## RESEARCH LETTER

10.1029/2019GL082382

### Key Points:

- We evaluate a fiber bundle model (FMB) that includes sintering and viscous deformation to model snow failure behavior
- The model can reproduce results of snow failure experiments, in particular the acoustic emission (AE) features and their rate dependence
- Though very simple, the model allows representing key mechanical features of snow by including sintering as well as viscous deformation

### Correspondence to:

A. Capelli,  
[achille.capelli@slf.ch](mailto:achille.capelli@slf.ch)

### Citation:

Capelli, A., Reiweger, I., & Schweizer, J. (2019). Modeling snow failure behavior and concurrent acoustic emissions signatures with a fiber bundle model. *Geophysical Research Letters*, 46. <https://doi.org/10.1029/2019GL082382>

Received 7 FEB 2019

Accepted 24 MAY 2019

Accepted article online 4 JUN 2019

©2019. The Authors.

This is an open access article under the terms of the Creative Commons Attribution-NonCommercial-NoDerivs License, which permits use and distribution in any medium, provided the original work is properly cited, the use is non-commercial and no modifications or adaptations are made.

## Modeling Snow Failure Behavior and Concurrent Acoustic Emissions Signatures With a Fiber Bundle Model

A. Capelli<sup>1</sup> , I. Reiweger<sup>2</sup> , and J. Schweizer<sup>1</sup>

<sup>1</sup>WSL Institute for Snow and Avalanche Research SLF, Davos Dorf, Switzerland, <sup>2</sup>Department of Civil Engineering and Natural Hazards, Institute of Mountain Risk Engineering, BOKU University of Natural Resources and Life Sciences, Wien, Austria

**Abstract** Snow failure is the result of gradual damage accumulation culminating in macroscopic cracks. The failure type strongly depends on the rate of the applied load or strain. Our aim was to study the microstructural mechanisms leading to the macroscopic loading rate dependence. We modeled snow failure and the concurrent acoustic emissions for different loading rates with a fiber bundle model and compared the model results to laboratory experiments. The fiber bundle model included two time-dependent healing mechanisms opposing the loading-induced damage process: (a) sintering of broken fibers and (b) relaxation of load inhomogeneities due to viscous deformation. The experimental acoustic emissions features could only be reproduced correctly if both healing mechanisms were included in the model. We conclude that both sintering and viscous deformation at a microscopic level essentially contribute to the macroscopic loading- and strain-rate dependent behavior of snow.

**Plain Language Summary** Snow slab avalanches originate from an initial crack in a weak snow layer followed by subsequent crack propagation within the snowpack. Understanding how this initial crack arises is essential for understanding the formation of spontaneous avalanches and subsequently also for avalanche hazard management. We used a numerical model mimicking the snow microstructure (fiber bundle model) to model snow failure experiments, where the load applied to the snow samples increased at different speeds until the samples failed. The crackling noise (or acoustic emissions) produced by the formation or growth of microscopic cracks within the snow was used to assess the damage process in the snow. We included in the model sintering and viscous deformation. Sintering means that two ice particles bond almost immediately upon contact, allowing the healing of cracks in snow. Viscous deformation means that ice deforms with time also at a constant force and, due to this, concentrations of forces in the snow are smoothed out over time. The model could reproduce the experiments only if both sintering and viscous deformation of ice were considered. We conclude that both mechanisms essentially contribute to snow failure and are of crucial importance for understanding snow failure and thus predicting avalanche release.

### 1. Introduction

In heterogeneous materials such as fiber composites, rocks, concrete, or snow, failure (the point when the material reaches its ultimate strength) may occur as the culmination of a progressive damage process. In other words, failure does not occur by a “one-crack” mechanism, but instead by the complex interactions between multiple defects and microcracks (Sornette, 2006, p. 313). During the damage process acoustic emissions (AE) are generated due to the formation as well as the growth of micro-cracks. Those AE can be used to study how failure develops (e.g. Grosse & Ohtsu, 2006) and in some cases to predict failure (e.g. Amitrano et al., 2005; Faillettaz et al., 2011).

Snow failure strongly depends on the speed of the imposed load. At rapid loading or deformation snow exhibits brittle failure behavior while for slow loading snow shows ductile failure behavior (Narita, 1980; Schweizer, 1998). A good understanding of the snow failure process is essential for modeling snow avalanche formation. In particular for the case of natural avalanches, the processes leading to initial crack formation are not fully understood.

By studying the AE generated in snow prior to failure, it is possible to shed light on the damage process preceding failure and the mechanisms controlling the loading rate dependence. Recently, Capelli, Reiweger, and Schweizer (2018) presented results of snow loading experiments with concurrent

measurements of the generated AE preceding failure. They found not only the failure behavior (brittle vs. ductile) but also the AE response to depend on the loading rate. At high loading rates, the exponent of the AE energy distribution ( $b$  value) decreased gradually and the AE energy rate increased exponentially. At low loading rates the exponent was almost constant and the exponential increase of the energy rate less pronounced. They suggested the observed differences in the AE signature to indicate a difference in the damage process. However, they could only hypothesize about the possible reasons since they had no model at hand to link the AE features to the damage process. Only with a model it seems possible to understand and interpret the AE signatures preceding snow failure and their dependence on the loading rate.

Snow consists of a highly porous ice matrix with air filling the pore space. The ice matrix can be described as discrete ice elements (grains) welded (sintered) together, as shown by microcomputed tomography (e.g., Coléou et al., 2001), and thus forming a heterogeneous structure. The form, size, and connectivity of the elements (microstructure) strongly influence the mechanical properties of snow (e.g., Mede et al., 2018; Schweizer et al., 2003). Moreover, the ice itself has peculiar mechanical properties due to its high homologous temperature under natural conditions. On contact two ice particles bond immediately (sintering), and the strength of the bond increases with time (Gubler, 1982; Szabo & Schneebeli, 2007). Furthermore, the ice undergoes viscous deformation (creep; e.g., Schulson & Duval, 2009; Sinha, 1978a, 1978b). Therefore, to model the damage process of snow, it is necessary to consider both the mechanical properties of ice and the complex interaction between the single elements of the ice matrix.

A possible class of models to describe snow failure are statistical models of failure such as the fiber bundle model (FBM; e.g., Kun et al., 2006). The FBM consists of a high number of single elements (fibers) with heterogeneous strengths, which obey simple mechanical (e.g., elastic deformation) and interaction (e.g., global vs. local load sharing) rules. From the interaction of the high number of single elements, the complex damage process of the bulk material is reproduced. A first attempt to model snow failure with a FBM was presented by Reiweger et al. (2009). They modeled displacement-controlled shear experiments and were able to reproduce the ductile-to-brittle transition that snow exhibits with increasing strain rate. This well-known rate dependence of snow strength (e.g., Narita, 1980; Schweizer, 1998) resulted from the different characteristic times they had selected for breaking and reforming bonds.

More recently, a new version of a FBM including two healing mechanisms, sintering and load relaxation, was suggested for modeling the mechanical behavior of snow (Capelli, Reiweger, Lehmann, & Schweizer, 2018). In their model, sintering counteracts the damage process creating new, load-supporting fibers and leads to an increase of the bundle strength without, however, changing the character of the failure with respect to the FBM without healing mechanisms. Load relaxation, which originates from the viscous deformation of the fibers, transfers load from the old fibers carrying more load to the fibers newly created by sintering. Apart from further increasing the strength of the system, load relaxation in combination with the effect of sintering changes the type of phase transition at failure with effects similar to the observed dependence of the AE signatures during snow failure experiments.

In this work, we combine the results of snow failure experiments (Capelli, Reiweger, & Schweizer, 2018) with the recently proposed FBM (Capelli, Reiweger, Lehmann, et al., 2018). We evaluate whether the suggested FBM, which includes sintering as well as load relaxation, can reproduce load-controlled snow failure experiments and the concurrent AE signatures, which were observed to depend on the loading rate. We aim to shed light on the damage process preceding failure and the mechanisms controlling the loading rate dependence. The understanding of the microscopic processes leading to macroscopic snow failure will contribute to better models describing snow avalanche formation.

## 2. Methods

### 2.1. Snow Failure Experiments

We performed loading experiments using quadratic snow samples with a side length of 50 cm and a height of about 10 cm. The layered snow samples included in the middle a weak layer consisting of depth hoar crystals, which was grown following the method described by Fukuzawa and Narita (1993). The samples were produced by sieving snow into three snow layers with different densities (middle [weak] layer

$\sim 150 \text{ kg/m}^3$  and top and bottom layers  $\sim 300 \text{ kg/m}^3$ ), which were then subjected to a temperature gradient of 1–1.5 K/cm for 7 days inducing snow metamorphism (faceting).

For the snow failure experiments the snow samples were clamped between two metal plates, and the load was increased linearly until the sample failed or the maximum load of 20 kPa was reached. We applied three different loading rates (32, 168, and 400 Pa/s). The samples were subjected to mixed-mode loading (shear and compression at  $35^\circ$ ), thus mimicking the situation on a typical avalanche slope. The applied load resulted in a progressive deformation of the samples, which was concentrated in the weak layer. At failure, a crack formed along the weak layer, and the weak layer eventually collapsed. Displacement and strain were obtained with particle image velocimetry from a video of the samples. During the loading process, the generated AE were recorded. The monitoring of AE allowed assessing the ongoing damage process preceding failure. The load-controlled snow failure experiments were described in detail by Capelli, Reiweger, and Schweizer (2018).

## 2.2. Fiber Bundle Model

In the following, we describe the main features of the FBM that was described in detail in Capelli, Reiweger, Lehmann, et al. (2018). The FBM consists of a set of  $N$  fibers subjected to a load  $\sigma$  increasing with loading rate  $\dot{\sigma}$ . The fibers have heterogeneous strengths mimicking the heterogeneity of snow. The fiber strength  $\sigma_{th}$  is drawn from a Weibull distribution:

$$p(\sigma_{th}|\mu, k) = k\mu^{-k}\sigma_{th}^{k-1}e^{-(\sigma_{th}/\mu)^k}. \quad (1)$$

The shape factor  $k$  controls the amount of disorder in the system, and  $\mu$  is a scaling factor. The load on the fibers is increased stepwise to the strength of the weakest fiber causing steps of variable duration  $\Delta t = \frac{\Delta\sigma}{\dot{\sigma}}$ . When the load on a fiber reaches its strength, the fiber fails, and the load is redistributed among the surviving fibers (democratic or global sharing). The load redistribution may cause failure of other fibers and possibly initiating a cascade or avalanche of fiber ruptures, which we will refer to in the following as a fiber rupture burst to avoid confusion to snow avalanches. The load increase eventually leads to the failure of the entire bundle when all fibers fail.

We added two features to this classical form of FBM:

- a In analogy to the sintering mechanism of ice, at each time step the broken fibers can heal (sinter) and regain full strength, which is independent from the previous fiber strength. The load is zero immediately after sintering and increases with the external load or with load redistribution. The same applies to the fiber strain. We assume that the probability of forming a new bond depends on the amount of damage (see Reiweger et al., 2009) and increases with time. Therefore, the probability  $p_{s,i}$  that a given broken fiber  $i$  resinters during the time interval  $\Delta t$  is

$$p_{s,i}(\Delta t) = \left(1 - e^{-\frac{\Delta t}{t_p}}\right) \frac{N_{\text{broken}}}{N} \quad (2)$$

and depends on the number of broken fibers  $N_{\text{broken}}$  as well as the characteristic sintering time  $t_p$ , which controls the speed of the sintering process.

- b We assume that the fibers are viscoelastic and each fiber can be described by a spring with elastic modulus  $E$  and a dashpot with viscosity  $\eta$  connected in series (Maxwell element). This viscoelasticity leads to time-dependent relaxation of the load inhomogeneities that arise since the resintered fibers do not carry load initially. More specifically, the viscous deformation leads to an exponential relaxation of the single fiber load  $\sigma_i$  to the mean fiber load  $\langle\sigma\rangle$  with

$$\sigma_i(t + \Delta t) = \langle\sigma\rangle + (\sigma_i(t) - \langle\sigma\rangle)e^{-\frac{\Delta t}{t_r}}, \quad (3)$$

with the characteristic relaxation time  $t_r = \frac{\eta}{E}$  controlling the relaxation speed.

The deformation of the fiber bundle is a superposition of elastic and viscous deformation. The strain  $\epsilon$  at the loading step  $J$  is obtained by the sum of the strain increases:

$$\epsilon_j(t) = \underbrace{\frac{1}{E} \sum_{j \leftarrow j} \frac{\dot{\sigma} \Delta t_j}{Z_j}}_{\text{load increase}} + \underbrace{\frac{\sum_{k \in S_j} \sigma_{k,j}}{U_j}}_{\text{redistribution}} + \underbrace{\frac{1}{\eta} \sum_{j \leftarrow j} \frac{\langle \sigma \rangle_j}{Z_j} \Delta t_j}_{\text{viscous part}} \quad (4)$$

where  $Z_j$  is the fraction of intact fibers,  $\sigma_{k,j}$  the load of the fibers  $k$ , and  $S_j$  the fibers that failed at the loading step  $j$ . The magnitude of the elastic part of the strain depends on  $\frac{1}{E}$  and the viscous part of the strain on  $\frac{1}{\eta}$ .

### 3. Model Calibration

We exemplarily compare the FBM model results with the result of failure experiments at three loading rates (400, 168, and 32 Pa/s) loaded at an angle of  $\alpha = 35^\circ$  (Capelli, Reiweger, & Schweizer, 2018). We will first discuss the physical meaning of the parameters governing the FBM and relate them to experimental values for snow. A comparison of the FBM with the experimentally observed failure behavior and the measured AE signatures will be presented in the next section. The strength of the fibers follows a Weibull distribution with the parameters  $\mu$  and  $k$  (equation (1)). The scale factor  $\mu$  controls the mean strength of the fibers ( $\langle \sigma_{th} \rangle$ ) and, therefore, the strength of the bundle. We adjusted  $\mu$  to fit the strength of the fiber bundle ( $\langle \sigma_{th} \rangle = 22.3$  kPa) to the strength of the snow samples. The shape factor  $k$  controls the amount of disorder in the system, and the disorder is higher for smaller  $k$ . The strength distribution should reflect the strength distribution of the elements of the ice matrix (bonds). Since no direct measurement method is available, we assumed the type of distribution and the value of  $k = 1.1$ , which gives the best fit to the experimental data.

The speed of the sintering process depends on the probability of creating new bonds (equation (2)), which is controlled by the amount of damage (number of broken fibers) and the sintering time  $t_p$ . The probability of sintering increases with the number of broken fibers  $N_{\text{broken}}$ , since we assume that in order to form a new bond, a broken fiber needs to meet another broken one. This assumption has been used before for modeling snow failure (Louchet, 2001) and for a FBM previously applied on snow (Reiweger et al., 2009). The strength of a new ice bond increases with time. Therefore, we assumed that some time is necessary until a new fiber can carry load. This is equivalent to introducing a time-dependent sintering probability governed by the sintering characteristic time  $t_p$ . For snow the characteristic time  $t_p$  is assumed to be constant (and therefore also the sintering speed), while the relationship between sintering and damage speed changes with the loading rate. The effects of sintering speed on the damage process are discussed in more detail in Capelli, Reiweger, Lehmann, et al. (2018). The parameter  $t_p = 20$  s was adapted to meet the loading rate for which a transition in the failure behavior of snow was observed for the experiments (between 32 and 168 Pa/s).

The relaxation speed is determined by the characteristic relaxation time that depends on the ratio of viscosity to elastic modulus  $t_r = \frac{\eta}{E}$ . Increasing the relaxation speed leads to faster load transfer from older fibers to younger fibers, which initially carry less load. The effects of relaxation speed on the damage process and failure behavior are discussed in more detail in Capelli, Reiweger, Lehmann, et al. (2018). Besides controlling the relaxation speed, the ratio of viscosity and elastic modulus also influences the bundle strain and its dependence on the loading rate (equation (4)). Therefore, the two parameters viscosity and elastic modulus need to be adapted to the measured strain and the observed failure behavior. We determined the elastic modulus and the viscosity fitting the stress strain relation and strain rate of the model to the measured curves for the lowest and fastest loading rate (see Figure 1) obtaining the best results with a characteristic relaxation time  $t_r = \frac{\eta}{E} = 2$  s.

Moreover, we compared the elastic modulus and viscosity used within the model with literature values of snow rather than ice since the strongly simplified structure of the FBM (unidirectional fibers) cannot reproduce the complexity of the ice structure of snow (Kirchner et al., 2001). Hence, the single fibers should be viewed as small discrete snow cells. Literature values of the elastic modulus of snow span over several orders of magnitude depending on snow density and type (e.g., Mellor, 1975). In addition, the measurement method has a strong influence on the reported values. Most methods provide an effective elastic modulus lower than the true Young's modulus, since the applied forces and deformation rates are not in the range where the deformation of snow is linear elastic (Reuter et al., 2019). The method providing best results for the elastic properties of snow is based on measuring the propagation speed of acoustic waves, which

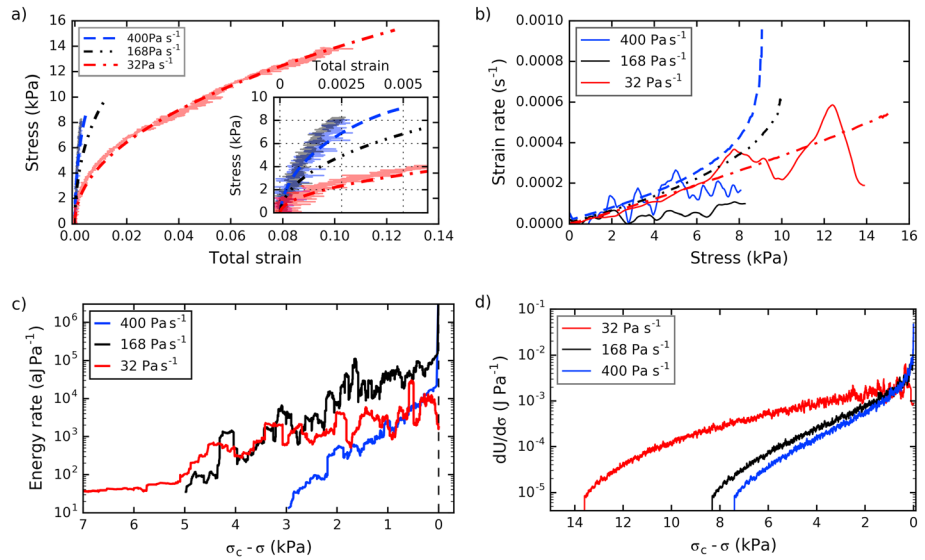


**Figure 1.** (a) Stress strain relations for both experiments (solid lines) and model (dash-dotted lines) for three different loading rates. The inset shows a magnification of the strain range between 0 and 0.005. (b) Strain rate as a function of the increasing stress for experiments (solid lines) and model (dash-dotted lines). (c) Evolution of AE energy rate  $\frac{dE_{AE}}{d\sigma}$  toward failure for three snow failure experiments with different loading rates. (d) Evolution of fiber bundle model elastic energy rate  $\frac{dU}{d\sigma}$  (emitted energy per unit stress) with increasing load. Events with energy lower than a given threshold ( $U < 10^{-9}$  J) are not taken into consideration, since in reality the sensitivity of the sensors is limited. Fiber bundle model size:  $N = 2.5 \times 10^5$ .

induce deformations that are small and fast enough to be in the elastic range (Capelli et al., 2016). Gerling et al. (2017) reported values of the elastic modulus in the range of 10–20 MPa for the density range of the weak layers of our samples ( $\sim 170$  kg/m<sup>3</sup>). The elastic modulus  $E = 19$  MPa we used for the FBM simulations is in agreement with the reported literature values (Gerling et al., 2017).

Also the literature values of snow viscosity vary widely. In addition to the expected dependence on snow density and type, snow viscosity also depends on temperature (Arrhenius type of relation), load (power law), and strain rate (power law; e.g., Mellor, 1975; Narita, 1983). These effects stem from the complexity of ice rheology. Therefore, it is evident that the assumption of linear viscous deformation is a strong simplification. However, considering that the applied load is in a relatively narrow range and the temperature was constant for all experiments ( $-5$  °C), the linear viscosity approximation seems sufficient for studying the basic effects of viscous deformation and the resulting load relaxation on the damage process and failure behavior. The viscosity value we used (37.5 MPa s) is within the range of values reported by Mellor (1975) for snow with a density of 170 kg/m<sup>3</sup> ( $\eta = 10$ – $10^3$  MPa s) considering that Mellor (1975) refers to compactive viscosity, whereas our experiments were performed in mixed-mode loading.

#### 4. Comparison of FBM and Experimental Failure Characteristics

The strain-stress relations of model and experiments are compared in Figure 1a. The higher strength and the higher strain at equal stress for low loading rates observed for snow were reproduced by the FBM. Moreover, the shape of the modeled stress-strain curves for low loading rates agrees well with the experimental curves. However, at low loading rates the model shows a divergence of the strain rate that was not observed in the experiments (Figure 1b). The strain rate divergence is caused by a divergence of the number of intact fibers carrying load and the resulting increase of the load per fiber (see also the discussion about the order parameter in Capelli, Reiweger, Lehmann, et al., 2018). The recorded acoustic energy  $E_{AE}$  is an indication of the amount of damage generated in the snow sample. Using the amount of energy per unit stress instead of energy per time allows comparing the increase of damage with increasing stress for the different loading rates. Hence, we refer to the energy rate as the energy rate of change with stress  $\frac{dE_{AE}}{d\sigma}$ . According to Hooke's

law the elastic energy stored in the fibers is  $U = \frac{\sigma_{\text{fiber}}^2}{2E}$  (e.g., Michlmayr et al., 2012; Pradhan & Hemmer, 2008). We hence assume that when the fibers fail, this elastic energy is dissipated partially as AE and that the AE energy  $E_{\text{AE}}$  produced by the microscopic damage is proportional to the elastic energy  $U$  stored in the breaking fibers. Therefore, we can compare the modeled elastic energy rate  $\frac{dU}{d\sigma}$  (Figure 1d) with the experimental energy rate  $\frac{dE_{\text{AE}}}{d\sigma}$  (Figure 1c). It needs to be noted at this point that the absolute values of the acoustic energy rates are difficult to compare, since the magnitude of the measured signals strongly depended on signal attenuation, the snow characteristics, and snow-sensor coupling quality. For the experiments we observed an exponential increase of the energy rate toward failure and the exponential coefficient (slope in Figure 1c) was higher for the higher loading rates. The model showed a similar behavior: an approximately exponential increase of the energy rate with increasing load (if the vicinity of the failure is disregarded) and a higher exponential coefficient at the higher loading rates. However, for the high loading rates the model showed a divergence of the energy rate close to failure, which has the same cause as the divergence of the strain rate.

The probability density functions of all events up to failure for the AE energy  $E_{\text{AE}}$  and modeled burst elastic energy  $U$  are shown in Figures 2a and 2b. We can assume that a large part of the modeled low energy failure bursts would not be recorded in reality, since AE recording is limited by sensor sensitivity, signal attenuation, and noise. Therefore, we considered only the tail of the distributions ( $E_{\text{AE}} \gtrsim 103$  aJ and  $U \gtrsim 10^{-7}$  J) in the following analysis. Both AE energy and elastic energy  $U$  were power law distributed, if just the highest energies were considered. The power law distribution  $P(E) \sim E^{-b}$  is usually observed for rupture events (e.g., Gutenberg-Richter law in seismology) and is characterized by the exponent that is usually referred to as the  $b$  value. Recent studies (Amitrano, 2012; Amitrano & Girard, 2016; Vu et al., 2019) suggest that the rupture event energy is in fact power law distributed with a cutoff energy  $E_0$ :

$$P(E) \sim E^{-\tau} \exp\left(-\frac{E}{E_0}\right). \quad (5)$$

The cutoff energy  $E_0$  increases with decreasing distance to failure  $\Delta = \frac{\sigma_c - \sigma}{\dot{\sigma}_c}$ :

$$E_0 \sim \Delta^{-\gamma}. \quad (6)$$

The three exponents are related to each other (Amitrano & Girard, 2016) as

$$b = \tau + \frac{1}{\gamma}. \quad (7)$$

The divergence of  $E_0$  causes an apparent decrease of the  $b$  value reaching the true exponent  $\tau$  at failure (Amitrano, 2012).

The evolutions of the distributions of  $E$  and  $U$  are shown in Figures 2c–2h. The  $b$  value was determined with a fit using the method described by Clauset et al. (2009) for all events (Figures 2a and 2b) and with a running window for the evolution approaching failure (insets Figures 2a and 2b). The  $b$  value of all events up to failure for the AE energy did not show a clear dependence on the loading rate, whereas for the FBM the  $b$  value was higher with lower loading rate. As described in Capelli, Reiweger, and Schweizer (2018), for the snow failure experiments a change in the AE energy distribution with an apparent decrease of the  $b$  value with increasing load was observed for the higher loading rates (400 and 168 Pa/s). For the slowest loading rate (32 Pa/s) the  $b$  value was almost constant. Moreover,  $\tau$  (or  $b$  value at failure) was higher for lower loading rates. The FBM showed similar results with apparent decreasing  $b$  value (Figure 2b) and higher  $\tau$  for slow loading. However, the  $b$  value of  $U$  at the lower loading rate was not constant but decreased toward failure. Using equation (6), the exponent  $\gamma$  can be calculated via  $b$  and  $\tau$ . The insets in Figures 2c–2h show the scaled energy distributions for the scaling factor  $\Delta^\gamma$  (equations (5) and (6) and Amitrano, 2012). For the high loading rates the scaled energy distribution curves collapsed for both the experiment and the FBM. This result corroborates the choice of power law with divergent cutoff assumption. The power law with divergent cutoff assumption seems not to be valid for the  $E_{\text{AE}}$  at lower loading range (Figure 2e), since we obtained  $\gamma = 21.2$ , an implausible result. In fact, the cutoff at high  $E_{\text{AE}}$  (bending of  $P(>E)$ ) is less pronounced at low loading rates. For the FBM with the low loading rate, the curves collapsed (Figure 2h).

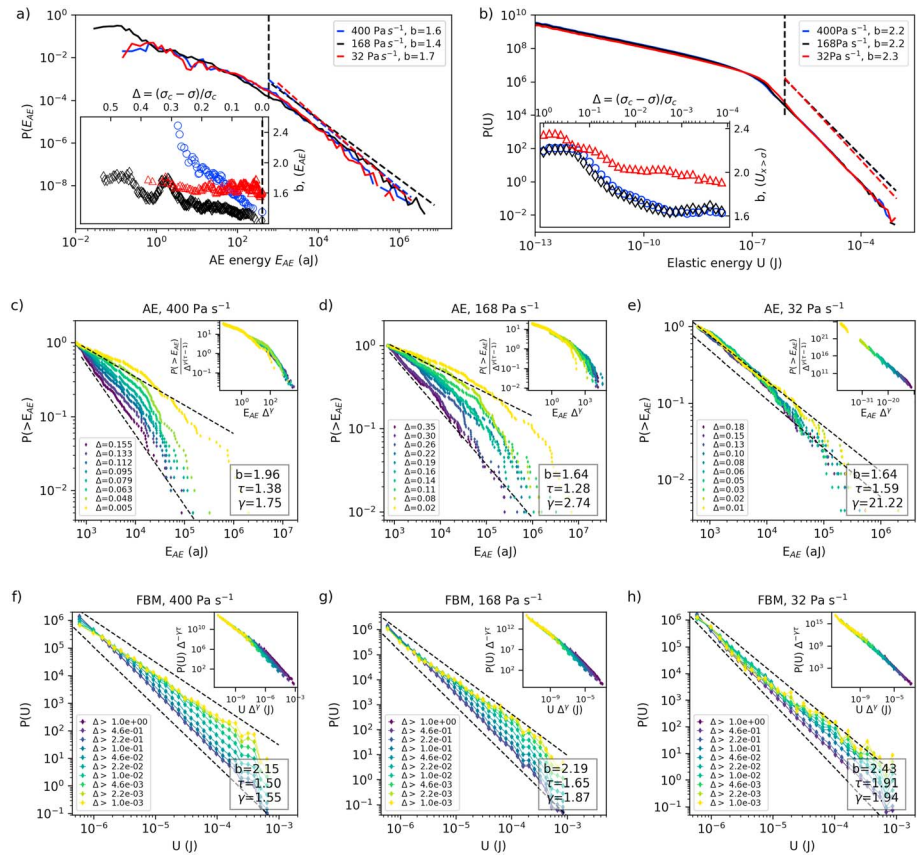


**Figure 2.** (a and b) Probability density functions of the acoustic emissions (AE) energy  $E_{AE}$  and the elastic burst energy  $U$  of all events up to failure for three different loading rates. The dashed lines indicate the power law fits for  $E_{AE} > 10^3$  aJ, and  $U > 8 \times 10^{-7}$  J. The corresponding  $b$  values are noted in the legends. The insets show the evolution of  $b$  value with increasing load  $\sigma$  up to failure at  $\sigma_c$  for three different loading rates for the AE energy  $E_{AE}$  and the fiber bundle model (FBM) burst elastic energy  $U$ . (c–h) Evolution of the  $E_{AE}$  (c–e) and  $U$  (f–h) distributions approaching failure for the different loading rates. The dotted lines show a power law with exponent  $b$  (bottom) and  $\tau$  (top). The insets show the rescaled plots (according to equations (5) and (6)) with the potential data collapse. To ensure correct statistics, we used 100 realizations of the FBM with size  $N = 9 \times 10^4$ .

## 5. Discussion and Outlook

We compared the FBM results with the stress-strain relations and AE features of snow failure experiments with different loading rates. The FBM reproduced quite well the loading rate-dependent results of the experiments using parameters in agreement with values found in literature. The model reproduced the observed higher strength and higher strain at equal stress at slow loading rates compared to fast loading rates, and the form of the experimental stress-strain relation at low loading rates. Moreover, the modeled AE features were similar to the experimentally observed AE. For both model and experiment the energy rate increased exponentially toward failure (except for the model with high loading rates close to failure), and the exponential coefficient (slope in Figure 1c) was higher for the higher loading rates. The FBM also reproduced well the observed characteristics of the energy distribution  $P(E_{AE})$  for the experiments with high loading rates and the higher exponent  $\tau$  observed for the experiments with lower loading rates. The higher exponent  $\tau$  at failure suggests that a different type of phase transition occurs at failure for the low loading rates. Such a difference in the failure behavior can be reproduced in the FBM only if both sintering and load relaxation are included in the model (Capelli, Reiweger, & Schweizer, 2018).

On the other hand, there were also some differences between model and experimental results. For the fast loading rates the FBM shows a divergence of the damage rate at failure, which results in the divergence of the strain rate (Figure 1b) and energy rate  $\frac{dU}{d\sigma}$  (Figure 1d), which was not observed for the experiments. Such a divergence has been previously reported for a FBM with equal load sharing and indicates a

second-order transition at failure (Pradhan et al., 2010). A divergence of the AE energy rate was observed for load-controlled laboratory experiments on composite materials (Guarino et al., 1998) and for collapse of limestone cliffs (Amitrano et al., 2005). Furthermore, a power law increase of the displacement velocity has been observed before break-off events from hanging glaciers (Faillettaz et al., 2016). An exponential increase of the energy rate is generally reported for displacement-controlled experiments where the imposed displacement prevents a divergence of the damage (Guarino et al., 1998; Salminen et al., 2002). A possible explanation for the missing divergence in the damage process for the snow experiments is that, for snow, failure occurred before the damage acceleration became visible in the acoustic energy rate. A mechanism that could induce such an early failure in the FBM is local load sharing (e.g., Faillettaz & Or, 2015; Hidalgo et al., 2002; Pradhan et al., 2010). A failure criterion assuming lower fiber strength at high strain rate, which mimics the brittle-to-ductile transition of ice (Schulson et al., 1984), may yield similar effects. Reducing the damage divergence at failure would improve the fit of the model to the stress-strain curve for high loading rates. Moreover, for the FBM model, the  $b$  value of  $U$  decreased with increasing load for the lowest loading rate, whereas the  $b$  value of the AE was constant for the lowest loading rate indicating a missing divergence of the cutoff energy.

The good agreement of modeled and experimental results is remarkable considering the simplicity of the model, and it confirms that the FBM is a valuable tool for studying the effects of basic microscopic mechanisms on the macroscopic failure behavior. Moreover, we showed that if we add viscous deformation and with it load relaxation, the FBM is capable of reproducing the observed loading rate dependence of the snow failure (e.g., larger strain at equal stress, no divergence, and higher  $\tau$  for low loading rates). As shown by Capelli, Reiweger, and Schweizer (2018) both sintering and load relaxation are necessary to correctly reproduce the AE features. Capelli, Reiweger, and Schweizer (2018) also discuss in detail the role the different mechanisms play. Many current models used for studying snow failure, however, do not consider any healing mechanism (Gaume et al., 2015) or consider only sintering (e.g., Gaume et al., 2017; Reiweger et al., 2009; Steinkogler et al., 2015). Our results show the necessity of considering both time-dependent mechanisms (sintering and load relaxation) for modeling snow failure at low loading rates (below  $\sim 100$  Pa/s for the snow type and conditions of our experiments) or for modeling natural snow avalanches where slow loading rates are involved.

The presented results have implications regarding the prediction of snow failure. The divergence of the damage rate at failure would allow identifying the failure point in advance. However, for the snow experiments and at low loading rates for the FBM, the divergence was not present. Similarly, the divergence of the cutoff energy connected with the apparent decrease of the  $b$  value, which would be as well a valid precursor (Amitrano, 2012; Amitrano et al., 2005; Capelli, Reiweger, & Schweizer, 2018), was not present for both experiment and FBM at low loading rates. This lack of clear precursors questions the feasibility of snow failure prediction, in particular for the release of natural dry-snow slab avalanches, which initially involve slow loading rates.

Our model is obviously still a simple representation of snow and its behavior. Possible improvements include substituting the linear viscosity by a power law relation for creep (Barnes et al., 1971; Kirchner et al., 2001) or introducing a sintering probability that depends on strain rate, hence reflecting the higher chance of building a new contact if the bundle experiences a higher strain.

As the FBM cannot reproduce the complex 3-D geometry of the ice matrix of snow, the two healing mechanisms could as well be implemented into other models, for example, a discrete element model. The discrete element model was used for simulating AE of porous rocks (Kun et al., 2014) and for simulating snow failure (Gaume et al., 2015; Mede et al., 2018). Finally, our findings may be applied to a slope scale model for studying natural avalanche release similar to the model of Fan et al. (2015) used for modeling landslide release.

## 6. Conclusions

We modeled snow failure experiments with a FBM. The experiments were performed at different loading rates and concurrently the AE were measured to study the influence of the loading rate on the progressive damage process prior to failure. The FBM included two healing mechanisms: (a) sintering that corresponds to regenerating broken fibers with time dependent probability and (b) viscous deformation of the fibers resulting in time-dependent relaxation of load inhomogeneities. Although our FBM is a strong

simplification of reality, the model proved to be useful for studying the basic effects of the two healing mechanisms on the damage process and failure behavior. The FBM allowed reproducing the loading rate dependent stress-strain relations observed in snow failure experiments. Moreover, the FBM exhibited AE features similar to the observed loading rate dependent AE features occurring before snow failure. Our results demonstrate that the FBM—if extended with viscous deformation and the resulting load relaxation—can reproduce load-dependent features observed in snow failure experiments, which previously could not be shown by using an FBM with only sintering of broken fibers. Hence, we conclude that both sintering and viscous deformation with resulting load relaxation are essential for understanding as well as modeling snow failure. These processes are of particular relevance when studying natural release of snow avalanches where slow loading conditions are involved.

### Acknowledgments

The data underlying Figures 1 and 2 are available on the EnviDat platform (<https://doi.org/10.16904/envidat.63>; <https://www.envidat.ch>). This project was funded by the Swiss National Science Foundation (SNF), project 200021-146647. We are grateful to Dani Or and Peter Lehmann for their comments. We further thank David Amitrano and an anonymous reviewer for their helpful reviews and suggestions for improvements.

### References

- Amitrano, D. (2012). Variability in the power-law distributions of rupture events—How and why does  $b$  value change. *European Physical Journal-Special Topics*, 205(1), 199–215. <https://doi.org/10.1140/epjst/e2012-01571-9>
- Amitrano, D., & Girard, L. (2016). Fiber bundle model under fluid pressure. *Physical Review E*, 93(3), 033003. <https://doi.org/10.1103/PhysRevE.93.033003>
- Amitrano, D., Grasso, J. R., & Senfaute, G. (2005). Seismic precursory patterns before a cliff collapse and critical point phenomena. *Geophysical Research Letters*, 32, L08314. <https://doi.org/10.1029/2004GL022270>
- Barnes, P., Tabor, D., & Walker, J. C. F. (1971). The friction and creep of polycrystalline ice. *Proceedings of the Royal Society of London. A. Mathematical and Physical Sciences*, 324(1557), 127–155. <https://doi.org/10.1098/rspa.1971.0132>
- Capelli, A., Kapil, J. C., Reiweger, I., Or, D., & Schweizer, J. (2016). Speed and attenuation of acoustic waves in snow: Laboratory experiments and modelling with Biot's theory. *Cold Regions Science and Technology*, 125, 1–11. <https://doi.org/10.1016/j.coldregions.2016.01.004>
- Capelli, A., Reiweger, I., Lehmann, P., & Schweizer, J. (2018). Fiber bundle model with time-dependent healing mechanisms to simulate progressive failure of snow. *Physical Review E*, 98(2), 023002. <https://doi.org/10.1103/PhysRevE.98.023002>
- Capelli, A., Reiweger, I., & Schweizer, J. (2018). Acoustic emissions signatures prior to snow failure. *Journal of Glaciology*, 64(246), 543–554. <https://doi.org/10.1017/jog.2018.43>
- Clauset, A., Shalizi, C. R., & Newman, M. E. J. (2009). Power-law distributions in empirical data. *SIAM Review*, 51(4), 661–703. <https://doi.org/10.1137/070710111>
- Coléou, C., Lesaffre, B., Brzoska, J.-B., Ludwig, W., & Boller, E. (2001). Three-dimensional snow images by X-ray microtomography. *Annals of Glaciology*, 32, 75–81. <https://doi.org/10.3189/172756401781819418>
- Faillettaz, J., Funk, M., & Sornette, D. (2011). Icequakes coupled with surface displacements for predicting glacier break-off. *Journal of Glaciology*, 57(203), 453–460. <https://doi.org/10.3189/002214311796905668>
- Faillettaz, J., Funk, M., & Vagliasindi, M. (2016). Time forecast of a break-off event from a hanging glacier. *The Cryosphere*, 10(3), 1191–1200. <https://doi.org/10.5194/tc-10-1191-2016>
- Faillettaz, J., & Or, D. (2015). Failure criterion for materials with spatially correlated mechanical properties. *Physical Review E*, 91(3), 032134. <https://doi.org/10.1103/PhysRevE.91.032134>
- Fan, L. F., Lehmann, P., & Or, D. (2015). Effects of hydromechanical loading history and antecedent soil mechanical damage on shallow landslide triggering. *Journal of Geophysical Research: Earth Surface*, 120, 1990–2015. <https://doi.org/10.1002/2015jf003615>
- Fukuzawa, T., & Narita, H. (1993). An experimental study on the mechanical behavior of a depth hoar under shear stress. Paper presented at the Proceedings ISSW 1992. International Snow Science Workshop, Breckenridge, Colorado, U.S.A., 4–8 October 1992.
- Gaume, J., Löwe, H., Tan, S., & Tsang, L. (2017). Scaling laws for the mechanics of loose and cohesive granular materials based on Baxter's sticky hard spheres. *Physical Review E*, 96(3), 032914. <https://doi.org/10.1103/PhysRevE.96.032914>
- Gaume, J., van Herwijnen, A., Chambon, G., Birkeland, K. W., & Schweizer, J. (2015). Modeling of crack propagation in weak snowpack layers using the discrete element method. *The Cryosphere*, 9(5), 1915–1932. <https://doi.org/10.5194/tc-9-1915-2015>
- Gerling, B., Löwe, H., & van Herwijnen, A. (2017). Measuring the elastic modulus of snow. *Geophysical Research Letters*, 44, 11,088–11,096. <https://doi.org/10.1002/2017GL075110>
- Grosse, C. U., & Ohtsu, M. (2006). *Acoustic Emission Testing*. Berlin, Germany: Springer.
- Guarino, A., Garcimartin, A., & Ciliberto, S. (1998). An experimental test of the critical behaviour of fracture precursors. *European Physical Journal B*, 6(1), 13–24. <https://doi.org/10.1007/s100510050521>
- Gubler, H. (1982). Strength of bonds between ice grains after short contact times. *Journal of Glaciology*, 28(100), 457–473. <https://doi.org/10.1017/S0022143000005050>
- Hidalgo, R. C., Moreno, Y., Kun, F., & Herrmann, H. J. (2002). Fracture model with variable range of interaction. *Physical Review E*, 65(4), 046148. <https://doi.org/10.1103/PhysRevE.65.046148>
- Kirchner, H. O. K., Michot, G., Narita, H., & Suzuki, T. (2001). Snow as a foam of ice: Plasticity, fracture and the brittle-to-ductile transition. *Philosophical Magazine A*, 81(9), 2161–2181. <https://doi.org/10.1080/01418610108217141>
- Kun, F., Hidalgo, R. C., Raischel, F., & Herrmann, H. J. (2006). Extension of fibre bundle models for creep rupture and interface failure. *International Journal of Fracture*, 140(1–4), 255–265. <https://doi.org/10.1007/s10704-005-2556-4>
- Kun, F., Varga, I., Lennartz-Sassinek, S., & Main, I. G. (2014). Rupture cascades in a discrete element model of a porous sedimentary rock. *Physical Review Letters*, 112(6), 065501. <https://doi.org/10.1103/PhysRevLett.112.065501>
- Louchet, F. (2001). Creep instability of the weak layer and natural slab avalanche triggerings. *Cold Regions Science and Technology*, 33(2–3), 141–146. [https://doi.org/10.1016/S0165-232X\(01\)00035-0](https://doi.org/10.1016/S0165-232X(01)00035-0)
- Mede, T., Chambon, G., Hagenmuller, P., & Nicot, F. (2018). Snow failure modes under mixed loading. *Geophysical Research Letters*, 45, 13,351–13,358. <https://doi.org/10.1029/2018GL080637>
- Mellor, M. (1975). A review of basic snow mechanics. Paper presented at the Symposium at Grindelwald 1974 - Snow Mechanics, IAHS Publ., 114.

- Michlmayr, G., Or, D., & Cohen, D. (2012). Fiber bundle models for stress release and energy bursts during granular shearing. *Physical Review E*, 86(6), 061307. <https://doi.org/10.1103/PhysRevE.86.061307>
- Narita, H. (1980). Mechanical behaviour and structure of snow under uniaxial tensile stress. *Journal of Glaciology*, 26(94), 275–282. <https://doi.org/10.1017/S0022143000010819>
- Narita, H. (1983). An experimental study on tensile fracture of snow. *Contributions from the Institute of Low Temperature Science*, A32, 1–37.
- Pradhan, S., Hansen, A., & Chakrabarti, B. K. (2010). Failure processes in elastic fiber bundles. *Reviews of Modern Physics*, 82(1), 499–555. <https://doi.org/10.1103/RevModPhys.82.499>
- Pradhan, S., & Hemmer, P. C. (2008). Energy bursts in fiber bundle models of composite materials. *Physical Review E*, (3), 77. <https://doi.org/10.1103/PhysRevE.77.031138>
- Reiweger, I., Schweizer, J., Dual, J., & Herrmann, H. J. (2009). Modelling snow failure with a fiber bundle model. *Journal of Glaciology*, 55(194), 997–1002. <https://doi.org/10.3189/002214309790794869>
- Reuter, B., Proksch, M., Löwe, H., van Herwijnen, A., & Schweizer, J. (2019). Comparing measurements of snow mechanical properties relevant for slab avalanche release. *Journal of Glaciology*, 65(249), 55–67. <https://doi.org/10.1017/jog.2018.93>
- Salminen, L. I., Tolvanen, A. I., & Alava, M. J. (2002). Acoustic emission from paper fracture. *Physical Review Letters*, 89(18), 185503. <https://doi.org/10.1103/PhysRevLett.89.185503>
- Schulson, E. M., & Duval, P. (2009). *Creep and fracture of ice*. Cambridge, UK: Cambridge University Press. <https://doi.org/10.1017/CBO9780511581397>
- Schulson, E. M., Lim, P. N., & Lee, R. W. (1984). A brittle to ductile transition in ice under tension. *Philosophical Magazine A*, 49(3), 353–363. <https://doi.org/10.1080/01418618408233279>
- Schweizer, J. (1998). Laboratory experiments on shear failure of snow. *Annals of Glaciology*, 26, 97–102. <https://doi.org/10.1017/S0260305500014634>
- Schweizer, J., Jamieson, J. B., & Schneebeli, M. (2003). Snow avalanche formation. *Reviews of Geophysics*, 41(4), 1016. <https://doi.org/10.1029/2002RG000123>
- Sinha, N. K. (1978a). Rheology of columnar-grained ice. *Experimental Mechanics*, 18(12), 464–470. <https://doi.org/10.1007/BF02324282>
- Sinha, N. K. (1978b). Short-term rheology of polycrystalline ice. *Journal of Glaciology*, 21(85), 457–474. <https://doi.org/10.1017/S002214300003361X>
- Sornette, D. (2006). *Critical phenomena in natural sciences*. Berlin, Germany: Springer-Verlag.
- Steinkogler, W., Gaume, J., Löwe, H., Sovilla, B., & Lehning, M. (2015). Granulation of snow: From tumbler experiments to discrete element simulations. *Journal of Geophysical Research: Earth Surface*, 120, 1107–1126. <https://doi.org/10.1002/2014jff003294>
- Szabo, D., & Schneebeli, M. (2007). Subsecond sintering of ice. *Applied Physics Letters*, 90(15), 151916. <https://doi.org/10.1063/1.2721391>
- Vu, C.-C., Amitrano, D., Plé, O., & Weiss, J. (2019). Compressive failure as a critical transition: Experimental evidence and mapping onto the universality class of depinning. *Physical Review Letters*, 122(1), 015502. <https://doi.org/10.1103/PhysRevLett.122.015502>